THE ASTRONOMICAL JOURNAL, 119:153–161, 2000 January

THE ORBITAL STRUCTURE AND POTENTIAL OF NGC 1399

R. P. SAGLIA,[1] ANDI KRONAWITTER,[2] ORTWIN GERHARD,[2,3] AND RALF BENDER[1]

Received 1999 April 15; accepted 1999 September 21

ABSTRACT

Accurate and radially extended stellar kinematic data reaching $R = 97''$ from the center are presented for the cD galaxy of Fornax NGC 1399. The stellar rotation is small ($\lesssim 30$ km s^{-1}); the stellar velocity dispersion remains constant at 250–270 km s^{-1}. The deviations from Gaussian line-of-sight velocity distributions are small, at the percent level. We construct dynamical models of the galaxy, deprojecting its nearly round (E0–E1) surface brightness distribution and determining the spherical distribution function that best fits (at the 4% level) the kinematic data on a grid of parameterized potentials. We find that the stellar orbital structure is moderately radial, with $\beta = 0.3 \pm 0.1$ for $R \leq 60''$, similar to results found for some normal giant elliptical galaxies. The gravitational potential is dominated by the luminous component out to the last data point, with a mass-to-light ratio $M/L_B = 10(M/L)_\odot$, although the presence of a central black hole of $M \approx 5 \times 10^8\ M_\odot$ is compatible with the data in the inner $5''$. The influence of the dark component is marginally detected starting from $R \approx 60''$. Using the radial velocities of the globular clusters and planetary nebulae of the galaxy, we constrain the potential more strongly, ruling out the self-consistent case and finding that the best-fit solution agrees with X-ray determinations. The resulting total mass and mass-to-light ratio are $M = 1.2\text{–}2.5 \times 10^{12}\ M_\odot$ and $M/L_B = 2-48(M/L)_\odot$ inside $R = 417''$ or 35 kpc for $D = 17.6$ Mpc.

Key words: celestial mechanics, stellar dynamics — dark matter — galaxies: elliptical and lenticular, cD — galaxies: individual (NGC 1399) — galaxies: kinematics and dynamics

1. INTRODUCTION

Determining the gravitational potential of elliptical galaxies and the amount of dark matter present is a notoriously difficult problem. This stems from the absence of extended cold gas that could be used as dynamical tracer and from the unknown intrinsic shape and orbital structure (see, e.g., Saglia 1996 and references therein). Progress has been made in recent years, thanks to improved observational data and dynamical modeling techniques.

On the one hand, we are now able to measure not only the stellar velocity and velocity dispersion profiles, but also the shape parameters of the line-of-sight velocity distributions with good accuracy (van der Marel & Franx 1993; Bender, Saglia, & Gerhard 1994, hereafter BSG94; Carollo et al. 1995; Gerhard et al. 1998a, hereafter G98; Statler & Smecker-Hane 1999). Such data contain information on the anisotropy and the gravitational potential (Gerhard 1993; Merritt 1993). On the other hand, algorithms based on Schwarzschild's (1979) orbit superposition technique (Rix et al. 1997; Cretton et al. 1999) or on the nonparametric reconstruction of the underlying distribution function (DF; G98; Matthias & Gerhard 1999) allow a detailed modeling of the data.

Until now, only a limited number of elliptical galaxies have been analyzed with these methods (Rix et al. 1997; G98; Matthias & Gerhard 1999). Nevertheless, the following pattern appears to emerge from these studies: out to 1–2 half-luminosity radii R_e, these objects are moderately radially anisotropic, and they have a dark component that starts to dominate the dynamics at about $R > 1\text{–}2R_e$. This is consistent with previous studies of extended velocity dispersion profiles of elliptical galaxies (Saglia, Bertin, & Stiavelli 1992; Saglia et al. 1993), of the radial velocities of globular clusters (GCs; Mould et al. 1990; Grillmair et al. 1994; Cohen & Ryzhov 1997; Minniti et al. 1998; Kissler-Patig et al. 1998) and planetary nebulae (PNs; Arnaboldi et al. 1994, 1998; Hui et al. 1995), and of the X-ray emission around elliptical galaxies (Ikebe et al. 1996; Jones et al. 1997) and, more recently, of the modeling of strong-lensing systems (Romanowsky & Kochaneck 1999) and the statistics of galaxy-galaxy lensing (Geiger & Schneider 1999).

In this paper we apply the nonparametric distribution-function reconstruction method to new, accurate, and extended data of the Fornax cD galaxy NGC 1399, to explore whether the conclusions reached for normal elliptical galaxies are valid also for the class of the most massive early-type galaxies. A preliminary description of the results can be found in Kronawitter et al. (1999). In the following we adopt a distance of 17.6 Mpc. NGC 1399 has been the subject of a number of dynamical studies in the past. Bicknell et al. (1989) analyzed the major-axis velocity dispersion profile using the Jeans equations, concluding that a constant mass-to-light ratio model with little anisotropy is able to reproduce the data out to $\approx 85''$. More recently, Graham et al. (1999a) reached the same conclusion using models based on $R^{1/n}$ luminosity profiles. X-ray observations indicate that the outer parts ($R > 120'' = 10.2$ kpc) are dominated by a dark halo that merges into the one of the Fornax Cluster at around $R \approx 53$ kpc (Ikebe et al. 1996). However, the potential inside $R \approx 10$ kpc is little constrained because of the presence of a cooling flow (Rangarajan et al. 1995). The radial velocities of globular clusters and planetary nebulae (see references above) agree with these mass determinations.

[1] Institut für Astronomie und Astrophysik, Scheinerstrasse 1, D-81679 Munich, Germany.
[2] Astronomisches Institut, Universität Basel, Venusstrasse 7, CH-4102 Binningen, Switzerland.
[3] Max-Planck-Institut für Astrophysik, Karl-Schwarzschild-Strasse 1, D-85740 Garching, Germany.

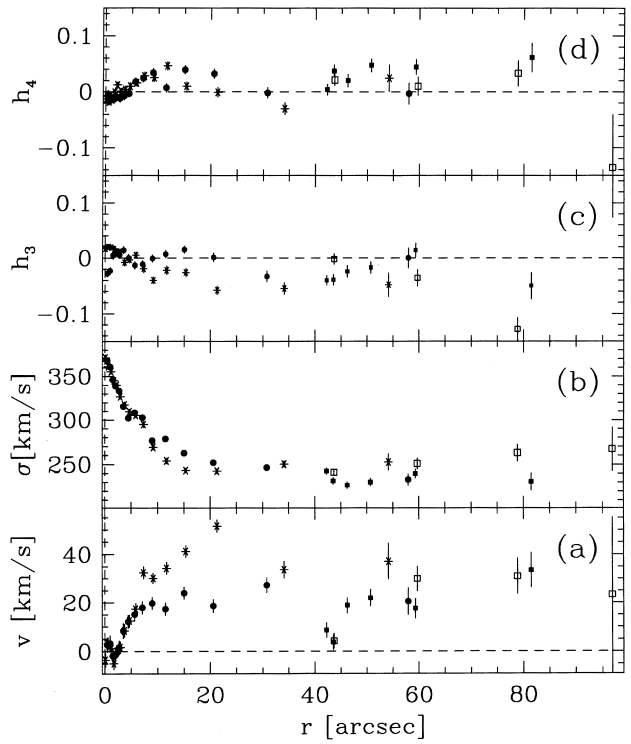

FIG. 1.—Kinematics of NGC 1399: (*a*) folded mean velocity, (*b*) velocity dispersion, (*c*) h_3, and (*d*) h_4 profiles. Asterisks and circles refer to the two sides of the galaxy and the major axis spectrum. Open and filled squares refer to the two sides of the galaxy and the spectra taken parallel to the minor axis and shifted 42″ from the center.

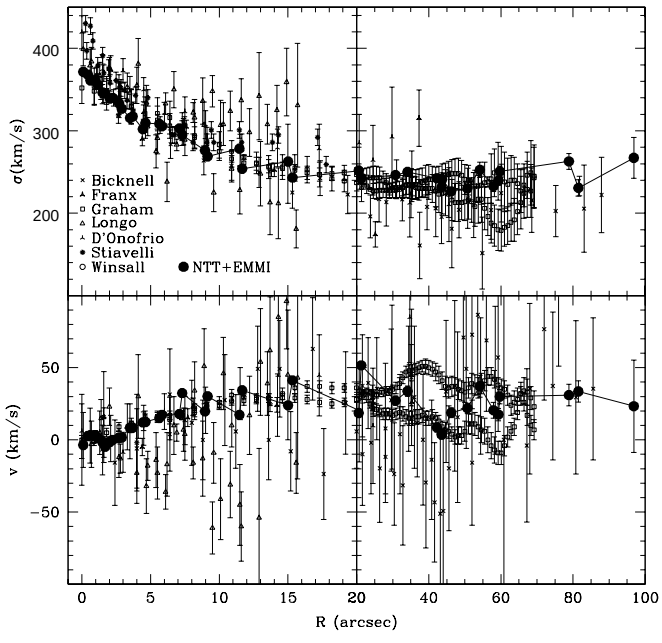

FIG. 2.—Comparison with the velocity dispersion (*top*) and rotation velocities (*bottom*) of Bicknell et al. (1989; *crosses*), Franx et al. (1989; *triangular diamonds*), Graham et al. (1998b; *squares*), Longo et al. (1994; *open triangles*), D'Onofrio et al. (1995; *triangular crosses*), Stiavelli et al. (1993; *stars*), and Winsall & Freeman (1993; *open circles*). The line connects the data points determined here (*filled circles*). Note the change of scale at $R = 20''$.

The structure of the paper is as follows: We present the data in § 2, where also the data reduction and the comparison with the literature are described and discussed. We review our dynamical modeling approach and discuss some modifications needed for the analysis of NGC 1399 in § 3. Results are presented in § 4, where the constraints from the absorption-line data are combined with those from GC and PN radial velocities and X-ray data. Conclusions are drawn in § 5.

2. OBSERVATIONS OF NGC 1399

The observations were performed 1994 December 6–8, using EMMI and the New Technology Telescope, in remote observing mode from Garching. The grating No. 6 (13.5 Å mm^{-1}) was used in combination with the ESO CCD Tektronix No. 36 (2048 × 2048 24 μm pixels, 0.″268 $pixel^{-1}$) and a 3″-wide slit, giving a FWHM spectroscopic resolution of 3.5 Å. The central wavelength was 5150 Å, giving 85 km s^{-1} σ_{inst} resolution; the spectral range (4826–5474 Å) covered the absorption lines Hβ, Mg, and Fe. A 1.5 hr–long spectrum was taken along the major axis of the galaxy (P.A. = 110°); additional 9 hr of integrations were taken parallel to the minor axis, shifting the slit 42″ from the center. Numerous template stars were also observed, wiggled, and trailed along the slit.

The standard reduction steps (bias subtraction, flat-fielding, cosmic-ray removal, logarithmic wavelength calibration, sky subtraction) were performed under MIDAS. A sky subtraction better than 1% was achieved. The analysis of the data was carried out using the Fourier correlation quotient method (Bender 1990), following BSG94 and G98. The spectra were rebinned along the spatial direction to obtain a nearly constant signal-to-noise ratio (S/N) of greater than 50 per resolution element. The effects of the continuum fitting and instrumental resolution were extensively tested by Monte Carlo simulations. The residual systematic effects on the values of the h_3 and h_4 profiles are less than 0.01, and less than 1.5% in σ. The error bars (which reflect the random errors and do not take into account systematic effects such as template mismatching or the presence of dust and faint emission; see below) are very small, in the range 3–7 km s^{-1} for the recession velocities and velocity dispersion, and 0.006–0.02 for the h_3 and h_4 coefficients. They are calibrated with simulations and are determined to better than 20%. They agree with the scatter of the points,-except for the five pairs of points with $5'' < R < 20''$. In this region the spectra on the two sides of the galaxy are slightly different, probably because of low-level emission. The Hα maps (Goudfrooij et al. 1994; Singh et al. 1995; Macchetto et al. 1996) show that the emission is patchy in the 10″–20″ region along the slit position. Dust is also present (Goudfrooij et al. 1994). Bicknell et al. (1989), who notice the same asymmetry, suggest that "old shells" might also be partly responsible. In the inner 1.″5, where σ increases to 370 km s^{-1}, there is still some template mismatching, which none of the 15 comparison stars are able to eliminate. The outermost data point has low signal, and only the mean velocity dispersion data points are reliable.

Figure 1 shows the kinematic profiles, including h_3 and h_4, with the major-axis data folded with respect to the center and the spectra parallel to the minor axis folded with respect to the major axis. The rotation along the major axis is small, $\lesssim 30$ km s^{-1}, and is present also along the position parallel to the minor axis. The velocities measured in the

inner 3″ might indicate the presence of a kinematically decoupled core. The velocity dispersion increases to ≈ 370 km s^{-1} in the inner 5″ and flattens to ≈ 250 km s^{-1} in the outer region. The antisymmetric deviations from a Gaussian profile as parameterized by the h_3 coefficients are slightly negative where rotation is detected (see BSG94). The symmetric deviations measured by the h_4 coefficients are smaller than 0.05 and mostly positive.

The comparison with the rotational velocities along the major axis of Bicknell et al. (1989), D'Onofrio et al. (1995), Franx, Illingworth, & Heckman (1989), Graham et al. (1998b), and Longo et al. (1994) is shown in the bottom panel of Figure 2. There is overall good agreement within the quoted errors. The systematic deviations observed for the outermost data points of Longo et al. (1994) and D'Onofrio et al. (1995) suggest that these data sets are probably affected by residual sky subtraction errors. The comparison with the dispersion profiles of Bicknell et al. (1989), D'Onofrio et al. (1995), Franx et al. (1989), Graham et al. (1998b), Longo et al. (1994), Stiavelli, Møller, & Zeilinger (1993), and Winsall & Freeman (1993) is shown in the top panel of Figure 2. There is overall agreement within the (usually large) error bars given by the authors. Systematic differences are observed in the inner 5″, where differences in seeing and slit width may play an important role. In the outer parts, the velocity dispersions of Bicknell et al. (1989) are systematically smaller than those of our data. However, our data agree well with Graham et al. (1998b) and with the point at $R \approx 80''$ measured by Winsall & Freeman (1993).

3. DYNAMICAL MODELING

The algorithm used to analyze the kinematic data presented above follows closely the technique discussed in detail by G98. Therefore, here we limit ourselves to summarizing its main features and the modifications we implemented to fit NGC 1399. In § 3.1, we focus on the modeling of the light distribution; in § 3.2, we concentrate on the nonparametric reconstruction of the DF.

3.1. *Deprojection of the Light Distribution*

The surface brightness (SB) data of NGC 1399 consist of three sets: in the innermost part we use V-band *Hubble Space Telescope* (*HST*) data from Lauer et al. (1995); the medium range is covered by ground-based B-band CCD data from Bicknell et al. (1989); and the outer part is covered by photographic V-band data from Schombert (1986). As described by Bicknell et al. (1989), we used the Schombert (1986) data shifted by 1.2 mag and from 57″ on outward. The *HST* data are also shifted by 0.8 mag and are used out to 10″. With an effective radius of 42″, according to Faber et al. (1989), the photometric data extend over 75 effective radii. [Note that Caon, Capaccioli, & D'Onofrio 1994 find $R_e \equiv (a_e b_e)^{1/2} = 127''$ by fitting their extended photometry. The determination of the total magnitude and effective radius of NGC 1399 is highly uncertain, since its light profile is very shallow in the outer regions. The exact value of R_e does not play a role in the following analysis.]

The SB profile deviates strongly from a de Vaucouleurs or Jaffe profile, being much brighter in the outer parts. Thus, contrary to NGC 6703, for which G98 could model the light distribution as a Jaffe (1983) profile, we must here determine the three-dimensional luminous density of NGC 1399 by deprojection.

NGC 1399 is nearly round (E0–E1). If we assume spherical symmetry, the deprojection of the SB profile $\Sigma(R)$ to a spatial luminosity density $j^{\rm lum}(r)$ is unique and is given by the standard Abel equation

$$j^{\rm lum}(r) = -\frac{1}{\pi}\int_r^\infty \frac{d\Sigma(R)}{dR}\frac{dR}{\sqrt{R^2 - r^2}}\,. \quad (1)$$

To avoid the amplification of noise, we follow Wahba & Wendelberger (1980), Scott (1990), and Gebhardt et al. (1996) and first smooth the data by finding the function $\Sigma(R)$ (expressed as thin-plate splines), which maximizes the logarithm M of likelihood $\mathscr{L}$,

$$M = \log \mathscr{L} = \sum_i \frac{[\log \Sigma_i - \log \Sigma(R_i)]^2}{\epsilon_i^2} - \lambda P(\Sigma)\,, \quad (2)$$

where Σ_i denotes the observed SB at projected radius R_i and ϵ_i is the measurement error. The second term on the right-hand side is a penalty function P [the second derivative of the SB profile $-2.5d^2 \log \Sigma/d(\log R)^2$], which penalizes oscillations in $\Sigma(R_i)$ induced by noise. The factor λ controls the degree of smoothing. We fixed it to 0.003, which allows us to reproduce smoothly the outer, noisy regions of the galaxy without affecting the inner, high-S/N data points. We also tried using the more objective generalized cross validation method to determine the smoothing parameter, but this did not give useful results for this inhomogeneous data set.

The smoothed SB profile is then deprojected using equation (1). The error introduced by this inversion can be checked by generating data from a known model and deprojecting. For SB data drawn from a Jaffe model (Jaffe 1983), with similar quality to the NGC 1399 data, the deviations between the known and the deprojected luminosity density profile are smaller than 0.5% rms. Figure 3 shows the surface brightness profile of NGC 1399 and that obtained by projecting the luminosity density model computed from our deprojection method. The differences are smaller than 0.05 mag arcsec^{-2} for most of the radial range, and smaller than 0.02 mag in the integrated luminosities.

The resulting density profile is rather shallow, with some intrinsic structure at large radii. This would be lost if we had fitted a parameterized model to the SB data; by contrast, the regression-inversion method described above does not smooth away intrinsic features or force the profile to a fixed asymptotic decrease in the outer parts, as is the case in many analytic models.

3.2. *Distribution Function*

To analyze the line-of-sight velocity profile data, we proceed in two steps (Merritt 1993; Rix et al. 1997; G98): First, the gravitational potential is kept fixed and the best-estimate distribution function is determined, in a least-squares sense. For ideal data, the solution to this problem in the spherical case would be unique (Dejonghe & Merritt 1992). Then, this process is repeated for different gravitational potentials to determine those for which a statistically good fit to the data can be achieved with positive DF. Because changing the gravitational potential has a different effect on the line profiles than does changing the anisotropy of the stellar orbits (see, e.g., Gerhard et al. 1998b), both can be constrained; i.e., only a limited range of potentials is consistent with the data.

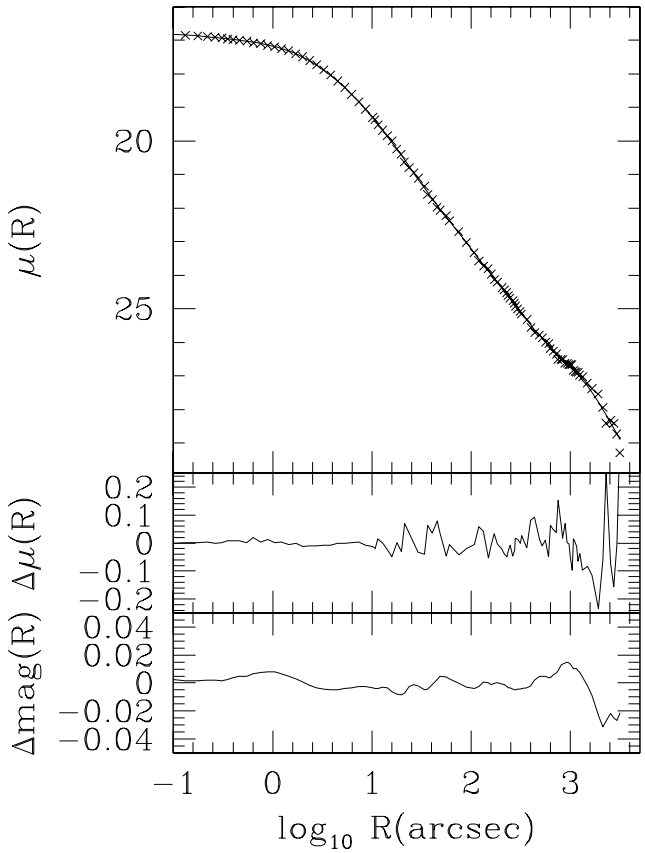

FIG. 3.—*Top*, combined surface brightness profile μ of NGC 1399 (*crosses*) and the projection of the derived luminous density model (*solid line*; see § 3.1); *middle*, residuals $\Delta\mu$ in magnitude per square arcsecond between the observed SB profile and the model; *bottom*, residuals Δmag in magnitude between the integrated luminosity of NGC 1399 and the model.

The potentials examined here are the sum of the potential of the luminous matter, obtained by solving Poisson's equation for the spherical luminosity density found in § 3.1, and that of a dark halo taken to be

$$\Phi^{\rm DM} = \tfrac{1}{2} v_0^2 \ln (r^2 + r_0^2) , \tag{3}$$

where v_0 is the asymptotic circular velocity and r_0 the core radius of the halo. We explored models with velocities v_0 from 0 (the self-consistent model) to 780 km s^{-1} and r_0 from $0.5R_e$ to $6.0R_e$. Models with these potentials minimize the contribution of the dark halo near the center and hence maximize the mass-to-light ratio of the luminous component. In this sense they are similar to the maximum disk models for spiral galaxies; by analogy we refer to them as *maximum stellar mass models*. A priori these halo potentials might not be correct; in fact, from cosmological simulations (Navarro, Frenk, & White 1997) one expects more centrally peaked halo distributions with asymptotic profiles at large radii $\propto r^{-3}$. However, the mass profiles derived from our approach match well the X-ray mass distribution (see Fig. 7 and § 4.3). In addition, the luminous density profile derived in § 3.1 is well approximated by a r^{-2} power law beyond 1″.

To recover the DF of a galaxy we construct a set of basis DFs in a fixed potential. Each basis DF has a different anisotropy structure and reproduces the luminous density profile determined as in § 3.1. The total DF is then a weighted sum of 57 of these basis functions:

$$f = \sum_k a_k f_k , \tag{4}$$

with $\sum_k a_k = 1$ and the additional constraint that $\sum_k a_k f_k \geq 0$ everywhere. For the basis functions f_k, we used sequences of tangentially anisotropic models, as described in § 4.1 and Appendix A of G98, as well as the isotropic model and a function with a radially anisotropic orbital structure. The radial function is used for determining the optimal velocity scales when computing the projected Gauss-Hermite moments for each of the f_k. The coefficients a_k are determined by fitting the projected model kinematics to the I data points such that

$$\Delta^2 = \sum_{k=1,I} (\chi^2_{\sigma,k} + \chi^2_{2,k} + \chi^2_{4,k}) + \lambda \sum_{i,j} \Lambda(f)_{i,j} \tag{5}$$

is minimal. Here χ^2_σ, χ^2_2, and χ^2_4 are as in equations (8) and (9) of G98 and measure the error-weighted square differences between the velocity dispersions of the galaxy and the model, and similarly for the second and fourth order Gauss-Hermite moments related to the measured h_4 coefficients. Following G98, we write the penalty function Λ as a combination of the second derivatives of the composite DF, evaluated on a grid of points (E_i, x_j) in the energy and circularity integrals. However, in the present case some care is needed in normalizing these second derivatives to avoid having a few data points dominate the regularization terms, because, as expected from the correlation between galaxy magnitude and the steepness of the central-profile slope (Faber et al. 1997), NGC 1399 has a rather shallow central cusp. Flat density profiles toward the center cause the distribution function, and similarly its second derivatives, to become very steep (Dehnen 1993). After testing different regularization functionals on simulated data of known distribution functions, we found that the best results are obtained by setting

$$\Lambda(f) = \frac{1}{(f''_{\rm iso})^2}\left(\frac{\partial^2 f}{\partial E^2}\right)^2 + \frac{2}{(f'_{\rm iso})^2}\left(\frac{\partial^2 f}{\partial E\,\partial x}\right)^2 + \frac{1}{(f_{\rm iso})^2}\left(\frac{\partial^2 f}{\partial x^2}\right)^2 , \tag{6}$$

where $f_{\rm iso}$, $f'_{\rm iso}$, and $f''_{\rm iso}$ are the isotropic DF and its first and second derivative with respect to energy.

The value of λ in equation (5) determines the degree of smoothness of the composite DF. Low values of λ result in a perfect fit to the data at the price of unphysical, small-scale variations in the DF. Large values of λ produce very smooth DFs that might not give acceptable fits to the data. We estimate the optimal value of λ by considering the composite DF recovered from Monte Carlo–simulated data, which are derived from an underlying distribution function similar to the one that gives the best fit to the NGC 1399 data, with the assumption of Gaussian errors (see G98 for details). Figure 4 shows the normalized total χ^2 of the fit to the artificial data and the percentage rms variations of the recovered DF, averaged over 25 realizations, as a function of λ. A potential with only the luminous matter and one including a halo with $r_0 = 168''$ and $v_0 = 427$ km s^{-1} are used for Figure 4. In both cases values around $\lambda \approx 0.01$ give $\chi^2 \approx 1$ and less than 15% mean rms variations of the DF. In the analysis of NGC 1399, we thus adopt $\lambda = 0.02$. Note that in G98 we found that slightly different values of λ were needed to fit the self-consistent and the halo potential cases. The difference here stems from the dominant role of the luminous component in NGC 1399 (see § 4.3).

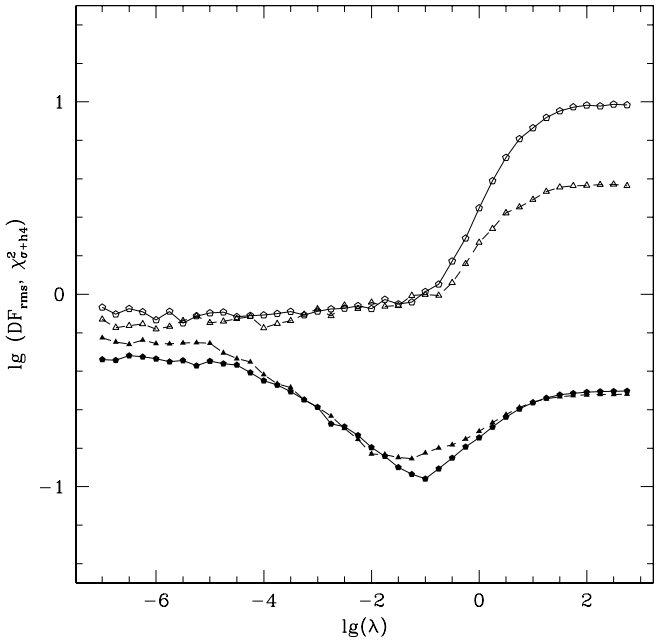

FIG. 4.—Model results as a function of the regularization parameter λ. The top two curves show the total χ^2 per σ and h_4 data point of regularized composite models with 57 basis functions. The bottom two curves show the rms deviation between the recovered composite model distribution function and the true distribution function from which the data sets were generated. This rms deviation was evaluated on a grid in energy and angular momentum corresponding to radii less than 3 times the radius of the outermost data point. Triangles refer to the self-consistent model, pentagons to a model in a halo potential with $r_0 = 168''$ and $v_0 = 427$ km s^{-1}.

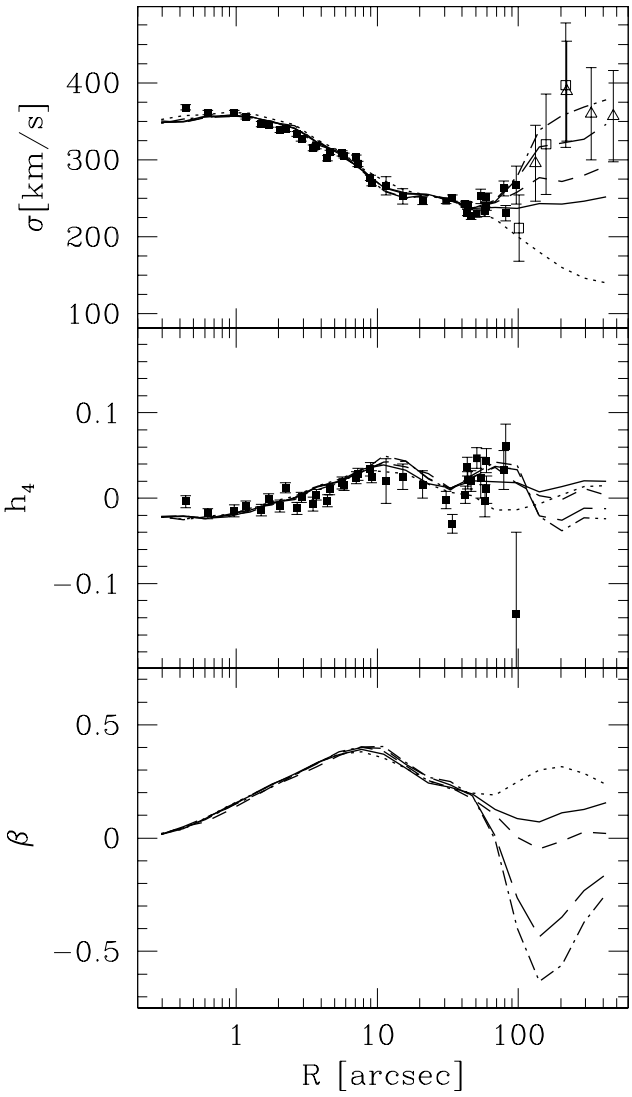

FIG. 5.—Dynamical models for the kinematics of NGC 1399 in several luminous plus dark matter potentials, compared with the measured projected velocity dispersion (*top*) and velocity profile shape parameter h_4 (*middle*). Solid, dashed, long-dashed, and dot-dashed lines, respectively, are the best-fit models with $V_{circ} = 383$, 404, 425, and 442 km s^{-1} at $R = 97''$. The dotted line is the self-consistent model with luminous matter only, $V_{circ} = 364$ km s^{-1}. Filled squares refer to the stellar kinematics, and open squares are the velocity dispersions derived for globular clusters, reduced by the factor 1.08 (see § 4.2). Open triangles are the velocity dispersions derived from planetary nebula velocities. The bottom panel shows the models' intrinsic anisotropy parameter $\beta(r)$.

Finally, we constructed cumulative χ^2 distributions for sets of 100 Monte Carlo simulations of our data set, drawn from radial and tangential models in self-consistent or halo potentials, respectively, and analyzed using $\lambda = 0.02$. We find that the 95% confidence level is reached at a value of $\chi^2 \approx 1.3$ per data point in all these cases. The same value results also when all errors are increased by 25%, with $\lambda = 0.02$ still being the optimal smoothing parameter. If we increase all errors by 40%, the 95% confidence level is reached at a value of $\chi^2 \approx 1.37$ per data point.

4. RESULTS

4.1. *Stellar Kinematics*

As discussed in § 2, the kinematic data show differences between the two sides of the galaxy significantly larger than the (small) statistical errors, probably because of low-level patchy emission. For radii $10'' < |R| < 22''$, we therefore use in the following the average values of σ and h_4 over the two sides, adopting as errors half of the side-to-side differences. In addition, while minimizing the square differences between models and data points over the whole radial range, we quote χ^2 values computed only from points at $|R| > 5''$. The velocity dispersion of NGC 1399 steeply increases to 370 km s^{-1} in the central 5″, which probably indicates the presence of a central massive object (Stiavelli et al. 1993). We explore models with central black holes at the end of this section.

The solid line in Figure 5 shows a dynamical model that best fits the kinematic data, obtained with a dark halo potential with $r_0 = 210''$ and $v_0 = 323$ km s^{-1}, corresponding to a total circular velocity $V_{circ} = 383$ km s^{-1} at the last data points, $R = 97''$. Fits of similar quality are obtained for a small range of model potentials; see the discussion in G98. Figure 5 shows three other models that span this range in the present case. These have circular velocities at the last data point of $V_{circ} = 404$, 425, and 442 km s^{-1}, respectively. All these models represent the data very well, with rms differences in σ of about 10 km s^{-1}, or 4.4%, and in h_4 of about 0.018 (excluding the last data point). The dotted line in Figure 5 shows the best model without dark halo ($V_{circ} = 364$ km s^{-1}); this has similar rms differences in σ and h_4 when only data points within 60″ are considered, but substantially larger values, 19 km s^{-1}, or 8.7% rms in σ, and 0.027 rms in h_4, when the data points at $R > 60''$ are included. Therefore we conclude that the gravitational

potential of the galaxy in the region probed by the absorption-line data is dominated by the luminous component but that the influence of the dark component is marginally detected starting at $R \approx 60''$.

Despite the excellent fit, the statistical interpretation of the resulting χ^2 values is not straightforward. The top panel of Figure 6 shows the values of the normalized global $\chi^2_{\sigma+h_4}$ obtained for the model fits, as a function of the circular velocity of the model at the last data point, $R = 97''$. Best-fit models are found in the range 380 km s^{-1} $< V_{\rm circ} <$ 450 km s^{-1} with values $\chi^2_{\sigma+h_4} \approx 1.9$, while the self-consistent model gives $\chi^2_{\sigma+h_4} \approx 3.7$. The Monte Carlo simulations of our data shown in Figure 4 demonstrate that the employed set of basis functions is sufficient to produce $\chi^2 \approx 1$, for a Gaussian error distribution and when the underlying model distribution function is similar to NGC 1399 and smooth. In these simulations, the 95% confidence limit corresponds to $\chi^2 \approx 1.3$. The rather high χ^2 values obtained for the real data set might partly be caused by an underestimation of the error bars. Fitting to the data for NGC 1399 with all error bars increased by 25% gives a normalized $\chi^2 = 1.3$ for our best-fitting model, just marginally acceptable in a statistical sense (see above). Only when all error bars are increased by 40% is the fitted model's χ^2 reduced to 1.06. However, the (statistical) uncertainty of the Monte Carlo–estimated error bars is not larger than 20% (see § 2), so most of the large χ^2 must be the result of systematic effects.

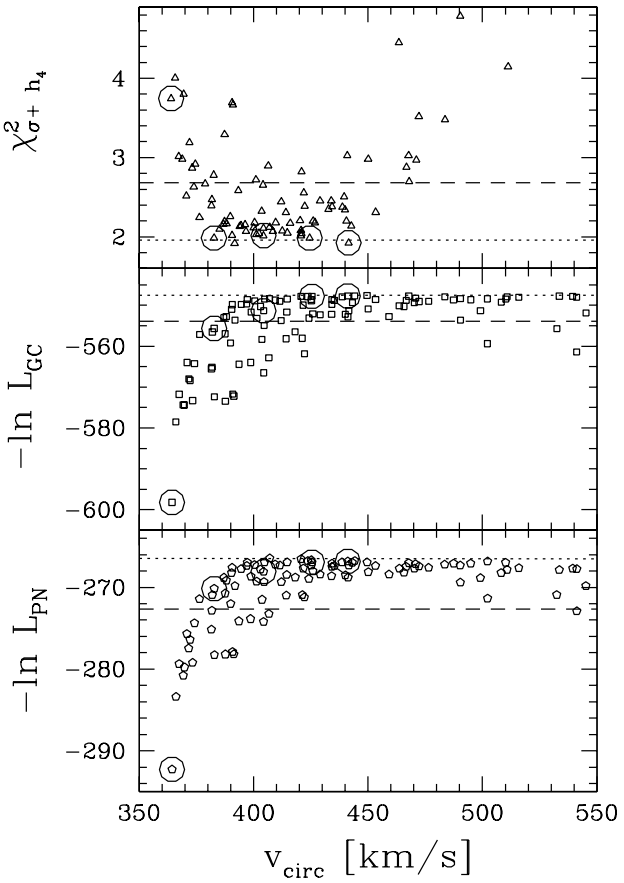

FIG. 6.—Quality of the kinematic model fits for NGC 1399 as a function of the true circular velocity at $R = 97''$. *Top*: normalized χ^2 of the fit to the $\sigma - h_4$ data points. The dotted line shows the mean χ^2 (scaled to the real errors) of the best models obtained from Monte Carlo simulations, when the errors are increased by 40% (see text). The dashed lines show the related 95% level, indicating an allowed range of $V_{\rm circ} = 420 \pm 40$ km s^{-1}. *Middle*: likelihood $-\ln \mathscr{L}_{\rm GC}$ of the globular cluster data set. *Bottom*: likelihood $-\ln \mathscr{L}_{\rm PN}$ of the planetary nebula data set. The models shown in Fig. 5 are circled. The dotted lines show the mean likelihood of the best models obtained from Monte Carlo simulations. The dashed lines show the 95% level.

Smaller, but still greater than unity, values of χ^2 are obtained if the two sides of the galaxies are fitted separately ($\chi^2 = 1.19$ and 1.58 for the two sides, using the original errors). This indicates that the systematic differences between the two sides discussed in § 2 are playing an important role. Also important are sudden point-to-point variations in the measured data values that are unlikely to be physical. We conclude that the residual differences (at the 2%–3% level) between model and data are of a systematic nature, with the most obvious candidates being dust, unresolved emission, local template mismatch, and slight oversmoothing of the model. This also suggests that we might have reached the intrinsic precision limit of stellar absorption-line measurements.

To estimate confidence intervals for the potential parameters, we therefore proceed as follows: We assume that, as a result of systematic effects, the real errors on our kinematic data points are 40% larger than the statistical errors determined from Monte Carlo simulations, so that the best-fitting model has a $\chi^2 \simeq 1$ per data point (the number of degrees of freedom is only slightly smaller than the number of data points because of the enforced regularization). The 95% confidence line is then at $\chi^2 = 1.37(1.4^2) = 2.68$, in units of the original errors; see Figure 6, top panel. The resulting 95% confidence range for the circular velocity at $R = 97''$ is $V_{\rm circ} = 420 \pm 40$ km s^{-1}. This is consistent with the sharp increase of the minimum values of χ^2 seen for $V_{\rm circ} < 380$ km s^{-1} and $V_{\rm circ} > 450$ km s^{-1}, which clearly indicates that this procedure gives a fair estimate for the range of allowed circular velocities for the combined luminous matter and halo potential. In this sense the four halo models shown in Figure 5 bracket the range of acceptable models.

The bottom panel of Figure 5 shows the anisotropy profiles derived for the different potentials discussed above. As a general trend, the profiles favor values of $\beta \approx 0.3$. The maximum at 10″ and sharp drop in the inner 5″ is uncertain (see discussion below), while the tendency of the most massive models to become tangentially anisotropic in the outer parts is also uncertain until confirmed by data at still larger radii; see § 4.2 and the discussion in G98. We conclude that NGC 1399 is slightly radially anisotropic with $\beta = 0.3 \pm 0.1$ out to $R = 60''$ or 5 kpc and that the anisotropy is not yet well constrained at larger radii. This is similar to what was found for NGC 6703 (G98) and NGC 2434 (Rix et al. 1997).

Finally, we briefly investigate the influence of the possible presence of a massive black hole on the inferred anisotropy in the center, without attempting a detailed analysis (this will be worthwhile only for data with *HST* resolution). We construct models with a central black hole of mass around $M = 5 \times 10^8$ $M_\odot$, which is approximately the mass expected for a galaxy of the luminosity of NGC 1399 (van der Marel 1999). We find that in these models the fit to the velocity dispersion profile in the inner 5″ follows the steep increase of the measured σ better, and the anisotropy change is milder. In models with massive black holes, the inferred anisotropy can be substantially changed even at 10″ and is slightly reduced at $\sim 20''$.

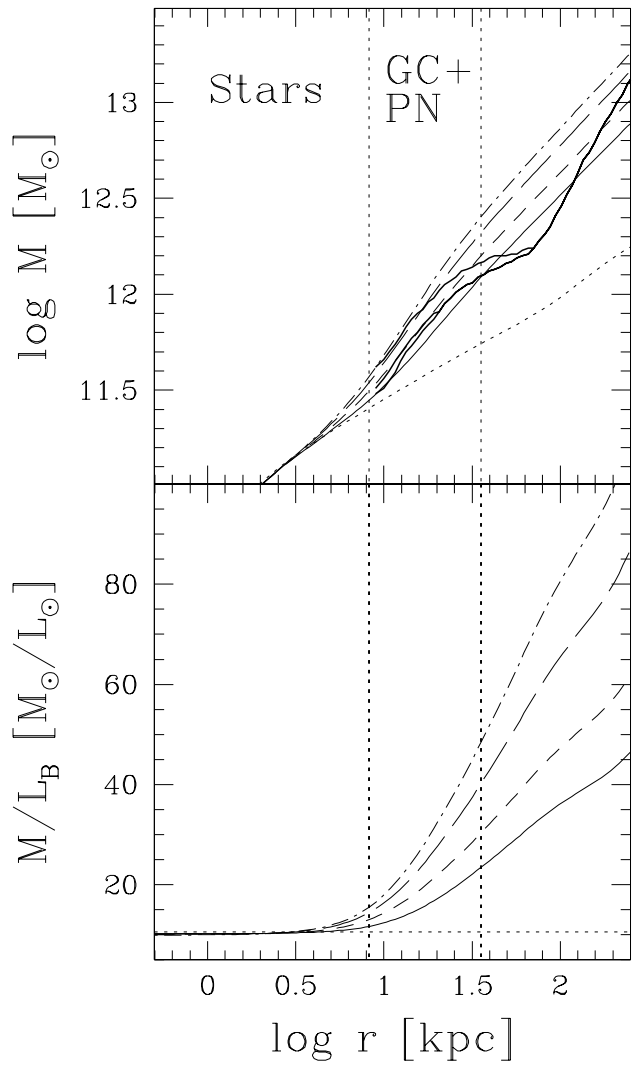

FIG. 7.—*Top*, total mass as a function of radius for the range of acceptable models for NGC 1399; *bottom*, mass-to-light ratio in the *B* band. Line styles are as in Fig. 5. The thick solid lines show the mass profiles derived from X-ray observations (see § 4.3).

4.2. *The Globular Cluster and Planetary Nebula Systems*

The mass distribution of NGC 1399 can be constrained further by considering its globular cluster and planetary nebula systems. Grillmair et al. (1994), Minniti et al. (1998), and Kissler-Patig et al. (1998) measured the radial velocities of 74 GCs, with typical errors of 100 km s^{-1}. Forbes et al. (1998) studied the radial distribution of the GCs and found that their surface density profile is flatter than the galaxy starlight, following a power law of slope $\gamma \approx -1.47$, 0.28 dex shallower than the galaxy. Thus at the same radius we expect the GCs to have a velocity dispersion $\sim(1.75/1.47)^{1/2} \approx 1.08$ larger than the stars of NGC 1399 (see, e.g., Binney & Tremaine 1987), assuming a logarithmic potential and a nearly isotropic DF for both components, which for the stars are approximately the case. The discussion below does not change if we ignore this small correction.

Arnaboldi et al. (1994) measured the radial velocities of 37 PNs, with typical errors of 50 km s^{-1}. The intrinsic density distribution of the PNs is not as well established as for the GCs. We assume that in the outer parts of NGC 1399 the density distribution of PNs follows that of the stars, with the same velocity dispersion. This is consistent with the histogram shown in McMillian, Ciardullo, & Jacoby (1993), but the number of PNs used is small and there is a possible selection bias from the coupled effects of the metallicity dependence of the specific density of PNs (Ciardullo & Jacoby 1992) and the observed color gradients in elliptical galaxies (Richer, McCall, & Arimoto 1997). Figure 5 shows the velocity dispersions (with their statistical errors) derived by binning radially the GC and PN velocities.

We proceed to compute the likelihood of the two data sets on our grid of gravitational potentials as follows: For each model we take the projected velocity dispersion profile $\sigma(R)$, as determined in § 4.1, and approximate the probability for measuring a given line-of-sight velocity at radius R_i by a Gaussian of zero mean and rms $= f\sigma(R_i)$, where $f = 1.08$ for the comparison with the GCs and $f = 1$ for the PNs. This simplifying assumption is justified by the low number of GC and PN velocities available and their rather large errors. Monte Carlo simulations showed that deviations from Gaussians can be detected only with samples of more than a few hundred measured velocities; see also Merritt (1997). After convolution with the (Gaussian) error distribution specified by the respective σ_i of each data point, we write the likelihood of the set of measured radial velocities v_i as

$$\mathscr{L}_{\rm GC} = \prod_{i=1}^{74} \frac{1}{\sqrt{2\pi[f^2\sigma^2(R_i) + \sigma_i^2]}} \times \exp\left\{-\frac{v_i^2}{2[f^2\sigma^2(R_i) + \sigma_i^2]}\right\}, \quad (7)$$

and similarly for $\mathscr{L}_{\rm PN}$. For comparison we also compute the likelihoods $\mathscr{L}_{\rm MC}$ of simulated sets of GC and PN radial velocities, generated from our best-fit model of NGC 1399.

The middle and bottom panels of Figure 6 show the results. Here we plot as a function of the circular velocity at $R = 97''$ the likelihoods of the models. In addition, we show two lines. The dotted line displays the mean value of the likelihood $-\ln\mathscr{L}$ for 100 Monte Carlo realizations of $N = 74$ GCs with velocities drawn from the projected kinematics of one of our best-fitting models (-547.6), and the same quantity (-266.45) for $N = 37$ PNs. The dashed line gives the 95% confidence level below which only 5% of the Monte Carlo realizations fall, for the GC (-553.9) and the PN (-272.5) samples. It is seen that the GCs and PNs favor the high-mass halo models of the range compatible with the absorption-line data and are inconsistent with the self-consistent model. The models that are best for the GC sample have $-\ln\mathscr{L}_{\rm GC} \approx -547$; they therefore give a good representation of the available data set. The same is true for the PN set. For both the GCs and the PNs, $\mathscr{L}_{\rm PN}$ decreases sharply for models with $V_{\rm circ} < 380$ km s^{-1}, in agreement with the results of § 4.1. The Monte Carlo simulations quoted above rule out the self-consistent model to almost certainty with either the GC or the PN sample. However, models with more massive halos than allowed by the stellar kinematics are compatible with the GC and PN data.

We have estimated the effect of a possible contamination of the GC and PN samples by intracluster objects. As suggested by Theuns & Warren (1997) and Mendez et al. (1997), some of the GCs and PNs considered above could in fact be foreground or background objects in the Fornax Cluster but not associated with NGC 1399. To test the

sensitivity of our results to such a contamination, we repeat the analysis on a subset of GCs and PNs where the 10% or 20% objects with the highest relative velocities have been eliminated. This is an extreme case, since we might expect some of the contaminators to have smaller velocities. We find that the results derived for the GC set are rather robust, with the best-fit potential remaining within the error range given above. However, when considering the PNs without the eight fastest objects, dark halos with circular velocities as low as $V_{\rm circ} \approx 350$ km s^{-1} are allowed. Velocities $V_{\rm circ} > 550$ km s^{-1} are also less favored.

4.3. *Mass and Mass-to-Light Distribution*

Figure 7 shows the permitted range for the cumulative mass distribution in NGC 1399, as derived from our combined fits to the absorption-line kinematics and the radial velocities of GCs and PNs. The dark matter contribution is negligible for $R \leq 60''$, or 5 kpc, and becomes progressively dominant at larger R. It comprises at most $\frac{1}{3}$ of the total mass at the last stellar kinematic data point, $R = 97''$ or 8 kpc, and 1–3 times the luminous mass at the radius of the most distant GC with a measured radial velocity $R \approx 417''$ or 35 kpc. Inside this radius, the allowed mass range matches the profiles derived from X-ray data by modeling the cooling flow (Ikebe et al. 1996), giving $M = 1.2 - 2.5 \times 10^{12}\ M_{\odot}$. At larger radii our simple models based on logarithmic halo potentials fail to follow the knee inferred from the X-ray data, which Ikebe et al. (1996) interpret as the transition of the galaxy potential to the Fornax Cluster potential. Nevertheless, these simple mass profiles are on the right mass scale even at these large distances.

The integrated mass-to-light ratio in the B band is approximately constant at $M/L_B \approx 10\ (M/L)_{\odot}$ out to $R \approx 60''$, increases to 12–15 at $R \approx 97''$, and reaches $M/L_B = 22 - 48\ (M/L)_{\odot}$ at $R = 417''$. Old ($t \geq 8$ Gyr) and metal-rich ($Z \geq 1\ Z_{\odot}$) stellar populations (Worthey 1994) can provide $M/L_B \approx 10$, matching at the same time the values of the Mg_2 index and $B-V$ color observed in the central regions of NGC 1399 ($Mg_2 = 0.334$, $B-V = 0.99$; Faber et al. 1989).

5. CONCLUSIONS

We have presented new accurate and extended stellar kinematic data for NGC 1399, the cD galaxy of the Fornax Cluster. Using a nonparametric algorithm, we have constructed smooth (at the 15% level) spherical distribution functions that reproduce the observed velocity dispersion and h_4 profiles at the 4% level. The models were tested for a grid of gravitational potentials, which combine a luminous part obtained from the deprojected surface brightness distribution with the assumption of constant M/L and a quasi-isothermal logarithmic dark halo potential. We have also explored the influence of a central black hole of mass $5 \times 10^8\ M_{\odot}$, finding that the steep increase in σ in the inner $5''$ can be better followed. We have further constrained the mass profile of the galaxy by taking into account the likelihoods of the radial velocities measured for the galaxy's globular cluster and planetary nebula systems and by comparing the results with the potential derived from X-ray measurements. Our main conclusions are summarized as follows:

1. The stellar orbital structure of NGC 1399 is moderately radial out to $R \approx 60''$, with $\beta = 0.3 \pm 0.1$, and is not yet well constrained at larger radii by the presently available data.
2. The luminous component of the galaxy dominates the dynamics out to $R \approx 60''$, with $M/L_B = 10\ (M/L)_{\odot}$. Old and metal-rich stellar populations reproduce this high value, matching also the measured values of the central $B-V$ color and Mg_2 index.
3. The influence of the dark halo is detected around $R \approx 60'' - 90''$ and becomes dominant in the region probed by the GC and PN systems, where the self-consistent model is ruled out.
4. The circular velocity at the last measured stellar kinematic point is $V_{\rm circ} = 380$–450 km s^{-1}. The corresponding mass profile range matches the mass curves derived from X-ray data with different assumptions to model the galaxy's cooling flow. Inside $R = 417''$ or 35 kpc, we derive $M = 1.2 - 2.5 \times 10^{12}\ M_{\odot}$ and a cumulative $M/L_B = 22 - 48\ (M/L)_{\odot}$.
5. The kinematics of the GCs and the PNs are consistent with those of the stars within the large statistical errors. The GCs appear slightly hotter, even when a correction for the different density profile slope is taken into account.

When compared with the normal giant elliptical galaxies where a detailed stellar dynamical analysis has been performed (NGC 1600, Matthias & Gerhard 1999; NGC 2434, Rix et al. 1997; NGC 6703, G98), the cD galaxy NGC 1399 appears to have a similar anisotropy profile inside the inner few kiloparsecs, with $\beta \approx 0.3$. The luminous component of the galaxy dominates the gravitational potential out to 8 kpc from the center. As judged from the GC and PN data, the transition to the dark matter dominated regime appears to be more rapid than in the case of NGC 6703. It is possible that this difference reflects the special position of NGC 1399 at the center of the Fornax Cluster. The best way to derive more stringent constraints on the nature of the transition region appears to be from larger samples of PN velocities such as can be obtained with the Very Large Telescope and other large telescopes.

The present analysis based on spherical models is adequate to study the very round inner regions of NGC 1399 considered here. For more flattened systems the methods developed by Matthias & Gerhard (1999) and Cretton et al. (1999) are the future ways to follow.

We thank M. Kissler-Patig for providing us with the globular cluster velocities in electronic form and the referee for constructive comments. R. P. S. and R. B. acknowledge the support by DFG grant SFB 375, A. K. and O. G. by grant 20-50676.97 from the Schweizerischer Nationalfonds. O. G. thanks the Max-Planck-Institut für Astrophysik for their hospitality during a sabbatical visit.

REFERENCES

Arnaboldi, M., Freeman, K. C., Gerhard, O. E., Matthias, M., Kudritzki, R. P., Méndez, R. H., Capaccioli, M., & Ford, H. 1998, ApJ, 507, 759
Arnaboldi, M., Freeman, K. C., Hui, X., Capaccioli, M., & Ford, H. 1994, Messenger, 76, 40
Bender, R. 1990, A&A, 229, 441
Bender, R., Saglia, R. P., & Gerhard, O. 1994, MNRAS, 269, 785 (BSG94)
Bicknell, G. V., Bruce, T. E. G., Carter, D., & Killeen, N. E. B. 1989, ApJ, 336, 639
Binney, J., & Tremaine, S. 1987, Galactic Dynamics (Princeton: Princeton Univ. Press)
Caon, N., Capaccioli, M., & D'Onofrio, M. 1994, A&AS, 106, 199
Carollo, C. M., de Zeeuw, P. T., van der Marel, R. P., Danziger, I. J., & Qian, E. E. 1995, ApJ, 441, L25
Ciardullo, R., & Jacoby, G. H. 1992, ApJ, 388, 268
Cohen, J. G., & Ryzhov, A. 1997, ApJ, 486, 230
Cretton, N., de Zeeuw, P. T., van der Marel, R. P., & Rix, H.-W. 1999, ApJS, 124, 383
Dehnen, W. 1993, MNRAS, 265, 250
Dejonghe, H., & Merritt, D. 1992, ApJ, 391, 531
D'Onofrio, M., Zaggia, S. R., Longo, G., Caon, N., & Capaccioli, M. 1995, A&A, 296, 319
Faber, S. M., et al. 1997, AJ, 114, 1771
Faber, S. M., Wegner, G., Burstein, D., Davies, R. L., Dressler, A., Lynden-Bell, D., & Terlevich, R. J. 1989, ApJS, 69, 763
Forbes, D. A., Grillmair, C. J., Willinger, G. M., Elson, R. A. W., & Brodie, J. P. 1998, MNRAS, 293, 325
Franx, M., Illingworth, G., & Heckman, T. 1989, ApJ, 344, 613
Gebhardt, K., et al. 1996, AJ, 112, 105
Geiger, B., & Schneider, P. 1999, MNRAS, 302, 118
Gerhard, O. E. 1993, MNRAS, 265, 213
Gerhard, O. E., Jeske, G., Saglia, R. P., & Bender, R. 1998a, MNRAS, 295, 197 (G98)
———. 1998b, in ASP Conf. Ser. 136, Galactic Halos, ed. D. Zaritsky (San Francisco: ASP), 248
Goudfrooij, P., Hansen, L., Jørgensen, H. E., & Nørgaard-Nielsen, H. U. 1994, A&AS, 105, 341
Graham, A., Colless, M., & Busarello, G. 1998a, in ASP Conf. Ser. 136, Galactic Halos, ed. D. Zaritsky (San Francisco: ASP), 257
Graham, A., Colless, M. M., Busarello, G., Zaggia, S., & Longo, G. 1998b, A&AS, 133, 325
Grillmair, C. J., Freeman, K. C., Bicknell, G. V., Carter, D., Couch, W. J., Sommer-Larsen, J., & Taylor, K. 1994, ApJ, 422, L9
Hui, X., Ford, H. C., Freeman, K., & Dopita, M. A. 1995, ApJ, 449, 592
Ikebe, Y., et al. 1996, Nature, 379, 427
Jaffe, W. 1983, MNRAS, 202, 995
Jones, C., Stern, C., Forman, W., Breen, J., David, L., Tucker, W., & Franx, M. 1997, ApJ, 482, 143
Kissler-Patig, M., Brodie, J. P., Schroder, L. L., Forbes, D. A., Grillmair, C. J., & Huchra, J. P. 1998, AJ, 115, 105
Kronawitter, A., Gerhard, O., Saglia, R. P., & Bender, R. 1999, in ASP Conf. Ser. 182, Galaxy Dynamics, ed. D. R. Merritt, M. Valluri, & J. A. Sellwood (San Francisco: ASP), 441
Lauer, T., et al. 1995, AJ, 110, 2622
Longo, G., Zaggia, S. R., Busarello, G., & Richter, G. 1994, A&AS, 105, 433
Macchetto, F., Pastoriza, M., Caon, N., Sparks, W. B., Giavalisco, M., Bender, R., & Capaccioli, M. 1996, A&AS, 120, 463
Matthias, M., & Gerhard, O. E. 1999, MNRAS, in press
McMillian, R., Ciardullo, R., & Jacoby, G. H. 1993, ApJ, 416, 62
Mendez, R. H., Guerrero, M. A., Freeman, K. C., Arnaboldi, M., Kudritzki, R. P., Hopp, U., Capaccioli, M., & Ford, H. 1997, ApJ, 491, L23
Merritt, D. 1993, ApJ, 413, 79
———. 1997, AJ, 114, 228
Minniti, D., Kissler-Patig, M., Goudfrooij, P., & Meylan, G. 1998, AJ, 115, 121
Mould, J., Oke, J. B., de Zeeuw, P. T., & Nemec, J. M. 1990, AJ, 99, 1823
Navarro, J. F., Frenk, C. S., & White, S. D. M. 1997, ApJ, 490, 493
Rangarajan, F. V. N., Fabian, A. C., Forman, W. R., & Jones, C. 1995, MNRAS, 272, 665
Richer, M. G., McCall, M. L., & Arimoto, N. 1997, A&AS, 122, 215
Rix, H.-W., de Zeeuw, P. T., Cretton, N., van der Marel, R., & Carollo, M. C. 1997, ApJ, 488, 702
Romanowsky, A. J., & Kochaneck, C. S. 1999, ApJ, 516, 18
Saglia, R. P. 1996, in IAU Symp. 171, New Light on Galaxy Evolution, ed. R. Bender & R. L. Davies (Heidelberg: Kluwer), 157
Saglia, R. P., et al. 1993, ApJ, 403, 567
Saglia, R. P., Bertin, G., & Stiavelli, M. 1992, ApJ, 384, 433
Schombert, J. M. 1986, ApJS, 60, 603
Schwarzschild, M. 1979, ApJ, 232, 236
Scott, D. W. 1990, Multivariate Density Function (New York: Wiley)
Singh, K. P., Bhat, P. N., Prabbu, T. P., & Kembhavi, A. K. 1995, A&A, 302, 658
Statler, T. S., & Smecker-Hane, T. 1999, AJ, 117, 839
Stiavelli, M., Møller, P., & Zeilinger, W. W. 1993, A&A, 277, 421
Theuns, T., & Warren, S. J. 1997, MNRAS, 284, L11
van der Marel, R. 1999, in ASP Conf. Ser. 182, Galaxy Dynamics, ed. D. Merritt, M. Valluri, & J. A. Sellwood (San Francisco: ASP)
van der Marel, R., & Franx, M. 1993, ApJ, 407, 525
Wahba, G., & Wendelberger, J. 1980, Mon. Weather Rev., 108, 1122
Winsall, M. L., & Freeman, K. C. 1993, A&A, 268, 443
Worthey, G. 1994, ApJSS, 95, 107